FBR for Polyolefin Production in Gas Phase: Validation of a Two-phase Compartmentalized Model by Comparison with CFD

(Article begins on next page)

FBR for Polyolefin Production in Gas Phase: Validation of a Two-Phase Compartmentalized Model by Comparison with CFD

Carmine Sabia,* Antonio Buffo, Tommaso Casalini, Daniele L. Marchisio, Maurizio C. Barbato, and Giuseppe Storti

Two different modeling approaches are applied in this work to the simulation of fluidized bed reactors containing solid particles of Geldart A-B type and operated at typical conditions for polyolefins production. On one side, a fully detailed computational fluid-dynamics (CFD) model is developed, considering a 2D planar geometry and a multi-fluid description with kinetic theory of granular flows. On the other, a conventional three-phase, 1D compartmentalized model (SCM) is also developed, implementing the fluid dynamic description based on popular, semi-empirical relationships available in the literature. Given the huge difference of computational effort associated with the corresponding numerical solutions, our aim is to confirm the reliability of the simplified model by comparison with the results of the detailed CFD model. The results show that the oversimplified compartmentalized approach is capable to predict the solid mixing features established inside the reactor operated in bubbling fluidization regime with good reliability for non-reactive polyethylene particles. Average solid volume fractions are particularly close to the values predicted by the CFD model when monodisperse particles are considered inside the examined range of gas velocity values. A generally good agreement is also found when solids with broad size distribution are analyzed.

1. Introduction

Fluidized bed reactors (FBRs) are the first-choice equipment for the gas phase production of polyolefins.[1,2] Modeling tools are extremely helpful to design the operating conditions in order to ensure the desired product quality, i.e., particle size and molecular weight distributions. Different modeling approaches have been proposed in the literature to simulate FBRs, ranging from multiscale kinetic models[3–6] to highly detailed computational-fluid-dynamics (CFD)-based models.[7,8]

Among the models of the first type, compartmentalized models are the most popular.[9–12] The reactor is described as combination of compartments (usually fully mixed) properly interconnected in order to simulate the fluid-dynamic behavior of the different phases. A major advantage of such an approach is that single particle models can be easily accounted for. Such equations allow for an adequate description of complex particle morphologies along with comprehensive kinetic polymerization schemes.[13] On the other hand, the description of the reactor fluid dynamics is based on empirical relationships (e.g., ref. [14]), whose applicability is often assumed a priori without further validation. In this respect, CFD simulations represent a major step forward in terms of detailed description of the hydrodynamic interaction between gas and solid particles.[15–17] Even though based on fundamental equations and advanced numerical methodologies, these approaches suffer the

C. Sabia, T. Casalini, M. C. Barbato
Department of Innovative Technologies
SUPSI
Via la Santa 1, Lugano 6962, Switzerland
E-mail: carmine.sabia@supsi.ch

C. Sabia, A. Buffo, D. L. Marchisio
Department of Science and Technology
Politecnico di Torino
Corso Duca degli Abruzzi 24, Torino 10129, Italy

T. Casalini, G. Storti
Department of Chemistry and Applied Biosciences
Institute for Chemical and Bioengineering, ETH Zurich
Vladimir-Prelog-Weg 1-5/10, Zurich 8093, Switzerland

G. Storti
Department of Chemistry
Materials, and Engineering Chemistry "Giulio Natta," Politecnico di Milano
Via Mancinelli 7, Milan 20131, Italy

ADVANCED SCIENCE NEWS
www.advancedsciencenews.com

[M] acro-molecular
Reaction Engineering
www.mre-journal.de

major limitation of huge computational effort, especially for 3D cases.[18–22] This practically prevents the use of similar tools in the industrial practice and limits the capability to include detailed descriptions of the particle size distribution and of the reaction features. In order to partly mitigate this issue, a pseudo-2D approach in which the third dimension is modeled as a thin thickness has been proposed but its application is nowadays limited to particular fields of study such as systems with a symmetry in which much of the phase motion evolves in 2D,[23] the development of novel drag models,[24] or the detailed description of phase heat transfer.[25]

The aim of this work is to assess a simple compartmentalized model implementing the conventional simplified fluid dynamic description by comparing the values of selected properties with those predicted by a detailed CFD model. The comparison between the two modeling approaches is carried out with reference to pure fluidization conditions, i.e., neglecting reaction and solid injection/withdrawal. Quantities like solid holdups, void fraction, and particle size distribution are compared to verify the reliability of the simplified approach and assess its use as effective design tool for practical applications, that is under reactive conditions. To the best of authors' knowledge, this is the first time such a comparison is carried out.

The scheme of the presentation is the following: i) development of the CFD model of FBR and its validation by comparison with literature results, ii) development of a standard three-phase compartmentalized model accounting for the particle size distribution of the solid particles, and iii) comparison between the predictions of the two models in terms of solid properties (volume fraction and average particle size) to assess the reliability of the simplified model with respect to the accurate predictions of the CFD simulations.

2. Development of the Multifluid CFD Model

In the multifluid model, gas (subscript g) and solid (subscript θ) phases are considered as interpenetrating continua in a full Eulerian framework. The gas phase is considered as primary phase while solid ones are defined as secondary or dispersed phases. The kinetic theory of granular flows (KTGF) is used to close the solid stress tensor terms.

2.1. Model Equations

In the case of no mass transfer mechanisms and no chemical reactions (usually represented through source terms), the continuity equations of gas and solid phase read[26]

$$\frac{\partial}{\partial t}\left(\alpha_g \rho_g\right) + \nabla \cdot \left(\alpha_g \rho_g \boldsymbol{u}_g\right) = 0 \tag{1}$$

$$\frac{\partial}{\partial t}\left(\alpha_\theta \rho_\theta\right) + \nabla \cdot \left(\alpha_\theta \rho_\theta \boldsymbol{u}_\theta\right) = 0 \tag{2}$$

where α_g and α_θ are the gas and solid phase volume fractions, ρ_g and ρ_θ are the gas and solid density, respectively, $\boldsymbol{u}_g$ is the velocity vector for the gas phase, and $\boldsymbol{u}_\theta$ is the solid phase velocity vector,

with θ ranging between 1 and N. The volume fraction of each phase is defined as

$$\alpha_i = \frac{V_i}{V} \tag{3}$$

where V_i is the volume occupied by phase i and V is the total volume. Due to the continuity constraint, the volume fractions have to sum to unity by definition

$$\alpha_g + \sum_{\theta=1}^{N} \alpha_\theta = 1 \tag{4}$$

The momentum transport equations for the gas and solid phases are

$$\frac{\partial}{\partial t}\left(\alpha_g \rho_g \boldsymbol{u}_g\right) + \nabla \cdot \left(\alpha_g \rho_g \boldsymbol{u}_g \boldsymbol{u}_g\right) = -\alpha_g \nabla p + \nabla \cdot \left(\overline{\overline{\tau}}_g\right)$$
$$+ \alpha_g \rho_g \boldsymbol{g} + \sum_{\theta=1}^{N} \boldsymbol{R}_{\theta g} \tag{5}$$

$$\frac{\partial}{\partial t}\left(\alpha_\theta \rho_\theta \boldsymbol{u}_\theta\right) + \nabla \cdot \left(\alpha_\theta \rho_\theta \boldsymbol{u}_\theta \boldsymbol{u}_\theta\right) = -\alpha_\theta \nabla p - \nabla p_\theta + \nabla \cdot \left(\overline{\overline{\tau}}_\theta\right)$$
$$+ \alpha_\theta \rho_\theta \boldsymbol{g} - \boldsymbol{R}_{\theta g} + \sum_{\vartheta=1; \vartheta \neq \theta}^{N} \boldsymbol{R}_{\vartheta \theta} \tag{6}$$

where $\overline{\overline{\tau}}_g$ and $\overline{\overline{\tau}}_\theta$ are the gas and solid phase stress–strain tensor, respectively

$$\overline{\overline{\tau}}_g = \alpha_g \mu_g \left(\nabla \boldsymbol{u}_g + \nabla \boldsymbol{u}_g^T\right) - \left(\frac{2}{3}\alpha_g \mu_g\right)\left(\nabla \cdot \boldsymbol{u}_g\right)\overline{\overline{I}} \tag{7}$$

$$\overline{\overline{\tau}}_\theta = \alpha_\theta \mu_\theta \left(\nabla \boldsymbol{u}_\theta + \nabla \boldsymbol{u}_\theta^T\right) + \alpha_\theta \left(\lambda_\theta - \frac{2}{3}\mu_\theta\right)\left(\nabla \cdot \boldsymbol{u}_\theta\right)\overline{\overline{I}} \tag{8}$$

Turbulence is modeled by solving the disperse formulation of the $k - \epsilon$ Re-Normalisation Group (RNG) turbulent model for the primary phase (Hartge et al.,[27] Loha et al.[28]):

$$\frac{\partial}{\partial t}\left(\alpha_g \rho_g k_g\right) + \nabla \cdot \left(\alpha_g \rho_g k_g \boldsymbol{u}_g\right) = \nabla \cdot \left(\alpha_g \|_k \mu_{eff,g} \nabla k_g\right) + \alpha_g G_{k,g}$$
$$+ \alpha_g G_{b,g} - \alpha_g \rho_g \epsilon_g + \alpha_g \rho_g \dot{\Pi}_{k_g} \tag{9}$$

$$\frac{\partial}{\partial t}\left(\alpha_g \rho_g \epsilon_g\right) + \nabla \cdot \left(\alpha_g \rho_g \epsilon_g \boldsymbol{u}_g\right) = \nabla \cdot \left(\alpha_g \|_\epsilon \mu_{eff,g} \nabla \epsilon_g\right)$$
$$+ \alpha_g C_{1\epsilon} \frac{\epsilon_g}{k_g}\left(G_{k,g} - G_{3\epsilon,g}G_{b,g}\right) - \alpha_g C_{2\epsilon}\rho_g \frac{\epsilon_g^2}{k_g} - \alpha_g R_\epsilon + \alpha_g \rho_g \dot{\Pi}_{\epsilon_g} \tag{10}$$

The particulate phase is described through the KTGF first developed by Chapman and Cowling[29] and Jenkins and Savage.[30] Granular temperature Θ_θ is introduced to model the random

**ADVANCED
SCIENCE NEWS**

www.advancedsciencenews.com

[M]acro-
molecular
Reaction Engineering
www.mre-journal.de

Table 1. KTFG equations and references.

Equation	Reference
$p_{\text{kin,coll}} = \alpha_\theta \rho_\theta \Theta_\theta + 2\alpha_\theta^2 \rho_\theta \Theta_\theta g_0 (1 + e_\theta)$	Lun et al.[31]
$p_{\text{fr}} = 0.05 \frac{(\alpha_\theta - \alpha_{\theta,\text{fr,min}})^2}{(\alpha_{\theta,\text{max}} - \alpha_g)^5}$	Johnson and Jackson[32]
$p_\theta = p_{\text{kin,coll}} + p_{\text{fr}}$	Johnson and Jackson[32]
$g_{0,\theta\theta} (\alpha_s) = [1 - (\frac{\alpha_s}{\alpha_{s,\text{max}}})^{\frac{1}{3}}]^{-1} + \frac{1}{2} d_\theta \sum\limits_{\theta=1}^{N} \frac{\alpha_\theta}{d_\theta}$	Lun et al.[31]
$\mu_{\text{kin,coll}} = \frac{4}{5} \alpha_\theta^2 \rho_\theta d_\theta g_{0,\theta\theta} (1 + e_\theta) (\frac{\Theta_\theta}{\pi})^{-\frac{1}{2}} + \frac{10 \rho_\theta d_\theta (\Theta_\theta \pi)^{\frac{1}{2}}}{96 g_{0,\theta\theta} (1 + e_\theta)} [1 + \frac{4}{5} (1 + e_\theta) \alpha_\theta g_{0,\theta\theta}]^2$	Gidaspow[33]
$\mu_{\text{fr}} = p_{\text{fr}} \frac{2^{\frac{1}{2}} \sin(\Phi_{\text{fr}})}{2(\boldsymbol{s}_\theta : \boldsymbol{s}_\theta)}$	Schaeffer[34]
$\mu_\theta = \mu_{\text{kin,coll}} + \mu_{\text{fr}}$	[35]
$\lambda_\theta = \frac{4}{3} \alpha_\theta^2 \rho_\theta d_\theta g_0 (1 + e_\theta) (\frac{\Theta_\theta}{\pi})^{-\frac{1}{2}}$	Lun et al.[31]

motion of particles and it is defined as one third of the mean square velocity fluctuations of solids:

$$\sqrt_\theta = \frac{1}{3} |\boldsymbol{u}'_\theta|\hat{2} \tag{11}$$

If granular energy does not vary remarkably with time and its dissipation takes place mainly locally, then the following algebraic expression can be written

$$0 = \left(-p_\theta \bar{\bar{I}} + \bar{\bar{\tau}}_\theta\right) : \nabla \boldsymbol{u}_\theta - \gamma_\theta \tag{12}$$

The KTGF model equations and relations, with detailed references, are summarized in **Table 1**.

The interaction between gas and the solid phases can be effectively modeled as the product of a coefficient $K_{\theta g}$ by the relative velocity between the gas and solid phase and adding its contribution to the momentum equations

$$\sum_{\theta=1}^{N} \boldsymbol{R}_{\theta g} = \sum_{\theta=1}^{N} \boldsymbol{R}_{g\theta} = \sum_{\theta=1}^{N} K_{\theta g} \left(\boldsymbol{u}_\theta - \boldsymbol{u}_g\right) \tag{13}$$

The same equation structure is used to consider the interaction between solid phases

$$\sum_{\theta=1}^{N} \boldsymbol{R}_{\vartheta\theta} = \sum_{\theta=1}^{N} \boldsymbol{R}_{\theta\vartheta} = \sum_{\vartheta=1; \vartheta \neq \theta}^{N} K_{\vartheta\theta} \left(\boldsymbol{u}_\vartheta - \boldsymbol{u}_\theta\right) \tag{14}$$

If particles with large inertia are considered (like in the case under examination), drag is the largely dominant body force and other contributions can be safely neglected. The Gidaspow model is usually employed to account for the fluid resistance in fluidized beds (Loha et al.,[28] Che et al.[36])

$$K_{\theta g} = \begin{cases} 150 \frac{\alpha_\theta^2 \mu_g}{\alpha_g^2 d_\theta^2} + 1.75 \frac{\alpha_\theta \rho_g |\boldsymbol{u}_\theta - \boldsymbol{u}_g|}{\alpha_g^2 d_\theta^2} & \text{if } \alpha_g \leq 0.8 \\ \frac{3}{4} C_D \frac{\alpha_\theta \rho_g |\boldsymbol{u}_\theta - \boldsymbol{u}_g|}{d_\theta} \alpha_g^{-2.65} & \text{if } \alpha_g > 0.8 \end{cases} \tag{15}$$

where C_D is the drag coefficient defined according to Naumann and Schiller[37]

$$C_D = \begin{cases} \frac{24}{\text{Re}_p} \left[1 + 0.15 \left(\text{Re}_p\right)^{0.687}\right] & \text{if } \text{Re}_p \leq 1000 \\ 0.44 & \text{if } \text{Re}_p > 1000 \end{cases} \tag{16}$$

$$\text{Re}_p = \frac{\alpha_g \rho_g d_\theta |\boldsymbol{u}_\theta - \boldsymbol{u}_g|}{\mu_g} \tag{17}$$

In addition to drag, the influence of the dispersed phase on the turbulence of the gas phase is accounted through the Simonin and Viollet model,[38] represented by the source terms Π_{k_g} and Π_{ε_g} expressed as

$$\dot{}_{k_g} = C_s \sum_{\theta=1}^{N} \frac{K_{\theta g}}{\alpha_g \rho_g} X_{\theta g} \left(k_{\theta g} - 2k_g\right) \tag{18}$$

$$\Pi_{\varepsilon_g} = C_{3\varepsilon} \frac{\varepsilon_g}{k_g} \Pi_{k_g} \tag{19}$$

where C_s is a model constant, usually set equal to 1, and $C_{3\varepsilon} = 1.2$. $K_{\theta g}$ is the covariance of the continuous and dispersed phase and $X_{\theta g}$ is a coefficient that for granular flows usually close to 1.[26,35] It is evaluated as

$$X_{\theta g} = \frac{\rho_\theta}{\rho_\theta + C_{\text{VM}} \rho_g} \tag{20}$$

with the added mass coefficient C_{VM} equal to 0.5.

Finally, the influence of turbulent interactions on the disperse phase has been considered through a modified viscosity for the secondary phases:

$$\nu_\theta = \frac{1}{3} k_{\theta g} \tau_{\theta g}^t + \frac{2}{3} k_\theta \tau_{\theta g}^F \tag{21}$$

2.2. Solution Algorithm

Simulations were performed using the cell-centered finite-volume code Fluent by ANSYS, Inc.[35] The highly turbulent

ADVANCED
SCIENCE NEWS
www.advancedsciencenews.com

{M} acro-molecular
Reaction Engineering
www.mre-journal.de

Table 2. Simulations boundary conditions.

Variable	Inlet	Outlet	Walls
$\boldsymbol{u}_g$	$\boldsymbol{u}_g \frac{\boldsymbol{n}}{|\boldsymbol{n}|}$	$\nabla \boldsymbol{u}_g \cdot \boldsymbol{n} = 0$	No slip
$\boldsymbol{u}_\theta$	0	$\nabla \boldsymbol{u}_\theta \cdot \boldsymbol{n} = 0$	Specified shear ($\tau = 0$)
α_θ	0	$\nabla \alpha_\theta \cdot \boldsymbol{n} = 0$	$\nabla \alpha_\theta \cdot \boldsymbol{n} = 0$
p_g	$\nabla p_g \cdot \boldsymbol{n} = 0$	p_{atm}	$\nabla p_g \cdot \boldsymbol{n} = 0$
k	$\frac{3}{2}(I|\boldsymbol{u}_g|)^2$	$\nabla k \cdot \boldsymbol{n} = 0$	Wall functions
ϵ	$\frac{C_\mu^{0.75} k^{1.5}}{L}$	$\nabla \epsilon \cdot \boldsymbol{n} = 0$	Wall functions

nature of the flow and its efficient mixing were described through the $k - \epsilon$ RNG turbulent model with the wall functions developed by Launder and Spalding.[39]

The coupling between pressure and velocity is obtained through the phase-coupled Semi-Implicit Method for Pressure Linked Equations (PC-SIMPLE) algorithm first developed by Patankar and Spalding[40] and later modified by Vasquez[41] to solve multiphase flow fields. Gradients are discretized through the green-gauss-node-based method (Barth and Jespersen[42]), while pressure is interpolated at cell faces using momentum equations coefficients as proposed by Rhie and Chow.[43] Following the work of Barth and Jespersen,[42] the spatial discretization for momentum and turbulent balances has been carried out by means of second-order accurate schemes, thus improving the predictions with respect to first-order schemes. The temporal dynamics of the system has been investigated by solving transient simulations discretized through bounded second-order implicit scheme with constant time step of 10^{-3} s, coherently to reference data (Che et al.[36]). Finally, all used boundary conditions are listed in **Table 2**.

3. Development of the Simplified Compartmentalized Model (SCM)

As discussed in previous literature,[2] many modeling approaches have been proposed to simulate this type of reactors, classified according to the number of phases accounted for and to the description of the reactor fluid dynamics. Among the different options, the well-assessed three-phase (two solid-rich and one pure gas) compartmentalized model originally proposed by Choi and Ray[44] and later applied by different authors[9,45,46] is used. Specifically, both the solid-rich phases (so-called emulsion and bubble wake) are compartmentalized as a series of continuous stirred tank reactors, with solid exchange between the two phases inside each compartment. Moreover, the particle size distribution of the solid product is considered in order to predict possible segregation phenomena along the reactor axis. Since the comparison performed in this work is focused on the fluidization behavior, we confine ourselves to nonreacting systems: therefore, the concentration profile along the reactor axis of preformed particles with given size distribution will be evaluated without including any specific polymerization kinetic and single-particle model. Of course, these additional aspects can be easily implemented in the proposed modeling framework if needed.

The conceptual schematization of the FBR as implemented in the compartmentalized model is shown in **Figure 1**. The reactor
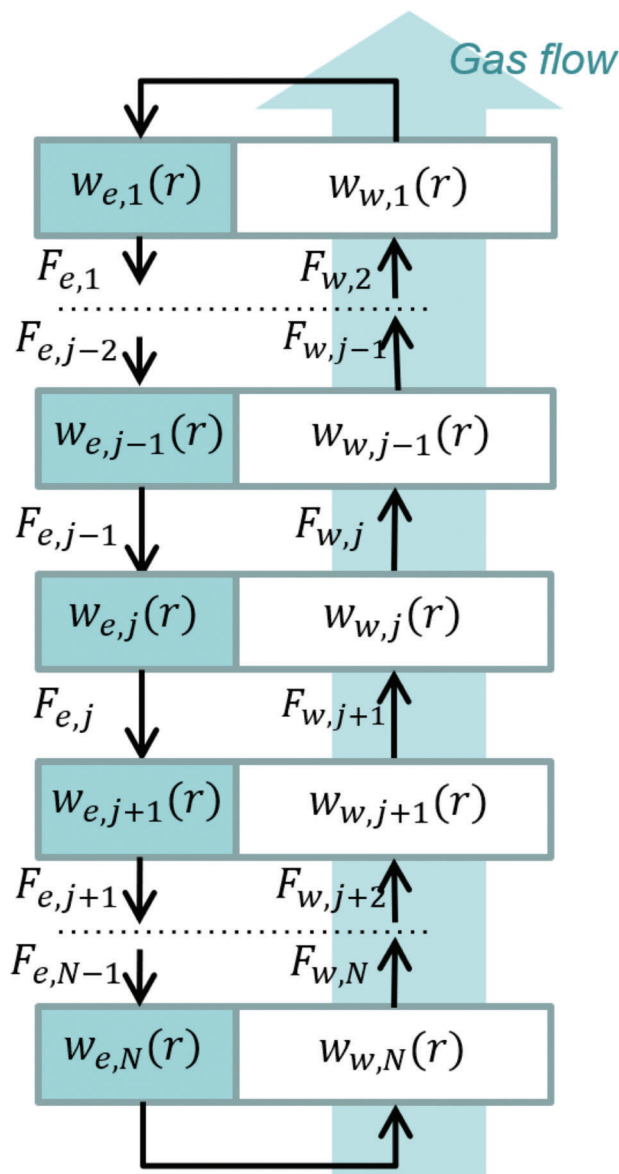

Figure 1. Schematic representation of the compartmentalized model. Black arrows; solid flows; light-blue arrow: pure gas flow.

is represented by a series of fully mixed compartments, each one containing two solid-rich phases, the emulsion flowing down, and the bubble wakes flowing up. The pure gas phase flowing up as bubbles is indicated by the big vertical arrow in the back. Inside each compartment, solid exchange between the two phases is taking place. The net rate of such exchange is evaluated as proposed by Kim and Choi,[47] with size-dependent rate coefficients of solid entrainment based on the exponential relationship proposed by Kunii and Levenspiel.[1]

3.1. Material and Population Balances

The steady-state model equations are summarized below.[46]

Table 3. Relationships applied to evaluate the simplified fluid dynamics.

Variable	Inlet	Equation
ϵ_{mf}	$0.586\phi_s^{-0.72}\left(\frac{\mu_g^2}{\rho_g\eta d_p^3}\right)^{0.029}\left(\frac{\rho_g}{\rho_p}\right)^{0.021}$ where $\eta = g(\rho_p - \rho_g)$	(30)
u_{mf}	$u_{mf}^2\frac{1.75\rho_g^2 d_p^2}{\epsilon_{mf}^3\phi_s\mu_g} + u_{mf}\frac{150(1-\epsilon_{mf})d_p\rho_g}{\epsilon_{mf}^3\phi_s^2} - \frac{\eta g d_p^3}{\mu_g} = 0$	(31)
u_t	$u_t^*\left(\frac{\rho_g^2}{\mu_g(\rho_p-\rho_g)g}\right)^{-1/3}$ where $u_t^* = \left(\frac{18}{d_p^{*2}} + \frac{2.335-1.744\phi_s}{d_p^{*0.5}}\right)^{-1}$ and $d_p^* = d_p\left(\frac{\rho_p(\rho_p-\rho_g)g}{\mu_g^2}\right)^{1/3}$	(32)
$d_b(z)$	$d_{b,m} - (d_{b,m} - d_{b,0})\exp\left(-\frac{0.3z}{d_t}\right)$ where $d_{b,m} = 0.652\left(\frac{\pi}{4}d_t^2(u_0-u_{mf})\right)^{0.4}$ and $d_{b,0} = \frac{2.78}{g}(u_0-u_{mf})^2$	(33)
$u_b(z)$	$u_0 - u_{mf} + u_{br}$ where $u_{br} = 0.711(gd_b)^{0.5}$	(34)
δ	$\frac{u_0-u_{mf}}{v_b-u_{mf}(\alpha+1)}$	(35)
α	$\alpha(d_p)$, see comment 4	(36)
$F_e(z)$	$v_b\alpha\delta(1-\epsilon_{mf})\rho_p\frac{\pi}{4}d_t^2$	(37)
$W_e(z)$	$(1-\alpha\delta-\delta)(1-\epsilon_{mf})\rho_p\frac{\pi}{4}d_t^2\Delta z$	(38)
$W_w(z)$	$\alpha\delta(1-\epsilon_{mf})\rho_p\frac{\pi}{4}d_t^2\Delta z$	(39)

– Mass balance in emulsion phase, j-th compartment

$$F_{e,j-1} - F_{e,j} = \bar{k}_{ew,j}W_{e,j} - \bar{k}_{we,j}W_{w,j} \tag{22}$$

– Population balances in emulsion phase, j-th compartment

$$F_{e,j-1}w_{e,j-1}(r) - F_{e,j}w_{e,j}(r) = k_{ew}(r)w_{e,j}(r)W_{e,j} - k_{we}w_{w,j}(r)W_{w,j} \tag{23}$$

– Mass balance in wake phase, j-th compartment

$$F_{w,j+1} - F_{w,j} = -\bar{k}_{ew,j}W_{e,j} + \bar{k}_{we,j}W_{w,j} \tag{24}$$

– Population balances in wake phase, j-th compartment

$$F_{w,j+1}w_{w,j+1}(r) - F_{w,j}w_{w,j}(r) = -k_{ew}(r)w_{e,j}(r)W_{e,j} + k_{we}w_{w,j}(r)W_{w,j} \tag{25}$$

where $F_{e,j}$ and $F_{w,j}$ are the solid mass flowrates of emulsion and wake leaving the compartment, $W_{e,j}$ and $W_{w,j}$ are the solid mass holdups of emulsion and wake of the same compartment, $w_{e,j}(r)$ and $w_{w,j}(r)$ are the particle size distributions in emulsion and wake on mass basis (weight fractions), and $k_{ew}(r)$ and $k_{we}(r)$ are the size-dependent rate coefficients of particle entrainment (emulsion to wake) and spillage (wake to emulsion), respectively. Note that the corresponding compartment-average rate coefficients appearing in the mass balances are readily evaluated as a function of the rate coefficients and the size distribution as

$$\bar{k}_{ew,j} = \int_0^\infty k_{ew}(r)w_{e,j}(r)\,dr \text{ and } \bar{k}_{we,j} = \int_0^\infty k_{we}w_{e,j}(r)\,dr \tag{26}$$

Assuming no solid elutriation, the following equalities apply to any pair of flowrates in between two adjacent compartments

$$F_{e,j-1} = F_{w,j} \text{ and } w_{e,j-1}(r) = w_{w,j}(r) \tag{27}$$

Plugging the last equation into Equation (23), the following relationship between the solid weight fractions of the particle of a given size is obtained

$$w_{e,j}(r) = \mathbb{C}_j(r)w_{w,j}(r) \tag{28}$$

where $\mathbb{C}_j(r) = (F_{e,j-1} + W_{w,j}k_{we}(r))/(F_{e,j} + W_{e,j}k_{ew}(r))$.

Given the number of compartments N as well as solid flowrates and holdups, Equation (28) ($j = 1, N$) along with the second Equation (27) ($j = 2, N-1$) are a system of $(2N-1)$ algebraic linear equations in the $2N$ unknowns $w_{e,j}(r)$, $w_{w,j}(r)$. The residual degree of freedom is readily saturated by imposing the consistency with the overall amount of solid particles of that size into the entire reactor, that is

$$w_{tot}(r)\sum_{j=1}^N\left(W_{e,j} + W_{w,j}\right) = \sum_{j=1}^N\left(W_{e,j}w_{e,j}(r) + W_{w,j}w_{w,j}(r)\right) \tag{29}$$

where $w_{tot}(r)$ is the particle size distribution (weight fraction) of the solid particles initially charged in the reactor. The solution of the resulting set of equations requires the evaluation of all flowrates and holdups, as discussed in the following section.

3.2. Simplified Fluid Dynamics

The description of the reactor fluid dynamics is based upon the semiempirical relationships reported by Kunii and Levenspiel[1] and summarized in **Table 3**. Note that the polymer particles under examination can be classified as Group A to B according to Geldart and Wong.[49,50]

Given the basic properties of gas (viscosity, μ_g, and density, ρ_g) and solid phase (density, ρ_p, average particle size, d_p, and sphericity, φ_s) of the generic compartment, key quantities such as the minimum fluidization gas velocity, u_{mf}, the corresponding void fraction, ϵ_{mf}, and the terminal velocity, u_t, are evaluated through Equations (30)–(32). Then, the bubble properties (size, d_b, and velocity, u_b) are estimated through Equations (33) and (34), while the void fractions specific of each phase (bubble fraction in the bed, δ, and wake fraction inside a bubble, α) are

**ADVANCED
SCIENCE NEWS**

www.advancedsciencenews.com

**M acro-
molecular
Reaction Engineering**

www.mre-journal.de

computed through Equations (35) and (36). Finally, the holdups of emulsion and wake are readily calculated by Equations (38) and (39) and the solid flowrate in emulsion leaving the compartment by Equation (37). Note that, according to the first Equation (27), the solid flowrate entering the same compartment as wake is identical.

A few comments about the selected relationships are required.

1) Spherical particles have been considered, i.e., $\varphi_s = 1$.
2) Given the average particle size, the superficial gas velocity u_0 will be set to values larger than u_{mf}, to ensure fluidization, and smaller than u_t to prevent elutriation.
3) The average bubble size is growing while traveling to the reactor top according to the exponential law (33). Since bubble breakage is expected above given size, the maximum value $d_{b,m}$ cannot overcome the limiting value suggested in [51,64] ($= 2u_t^2/g$, with g equal to the gravitational acceleration). Accordingly, the bubble size predicted by Equation (33) is set equal to such threshold value as soon as becoming larger.
4) The value of the wake fraction inside the bubble, α, is usually constant and equal to 0.4. For larger accuracy, data reported as a function of the average particle size in Figure 8 of Chapter 5 of ref. [1] have been used after interpolation.
5) Since most properties are function of the axial position inside the reactor, their evaluations have been carried out for each compartment considering its mid-point axial position, assuming such value representative of the entire compartment, while the Δz in Equations (38) and (39) is the compartment height.

3.3. Solution Algorithm

Given the reactor geometry (height and diameter), the size distribution of the solid particles charged to the reactor, $w_{tot}(r)$, and the inlet gas velocity, u_0, the numerical solution of the compartmentalized model is carried out iteratively as follows.

1) Given a first guess average particle size (usually estimated from the particle size distribution $w_{tot}(r)$), the equations in Table 3 are used to evaluate the axial profile of bubble size.
2) The compartment size is then estimated in order to include at least one entire bubble, that is, the compartment dimension is growing from bottom to top along the reactor axis.
3) Solid flowrates and holdups are evaluated through the relationships in Table 3 for each compartment.
4) Once evaluated $\bar{k}_{ew,j}$ for each compartment through the first Equation (26), the corresponding overall rate coefficient of particle spillage is calculated as

$$\bar{k}_{we,j} = \frac{\bar{k}_{ew,j} W_{e,j} - F_{e,j-1} + F_{e,j}}{W_{w,j}} \tag{40}$$

from which the value of $\mathbb{C}_j$ is readily obtained.
5) Then, the particle size distributions in emulsion and wake for each compartment are calculated from Equations (27)–(29) at each desired value of the particle size, that is ranging from the minimum to the maximum size according to the injected size distribution.

6) Given the distributions, the entire procedure is repeated from step 2 until convergence criteria are met. Such convergence has been conveniently quantified comparing the $\bar{k}_{we,j}$ values predicted by two following iterations.

4. CFD Test Case and Simulation Model

4.1. Model Validation

In absence of experimental data, the physical and numerical setup adopted has been validated against relevant literature data obtained from the work of Che et al.[36] The reactor geometry, reported in **Figure 2**, has been reproduced and simulation settings have been chosen to replicate the multiphase flow field taken as reference.

A quasi-steady-state fluidized bed is examined, assuming constant temperature, no chemical reactions, and no solid feed and withdrawal. This corresponds to the stable condition established in FBR after expansion of the initially charged amount of solid with given particle size distribution.

Although the flow features in fluidized beds are tridimensional, it is very usual to model the fluidization process using 2D computational domains since good results are obtained at a more reasonable computational cost, as shown by Gidaspow and Ettehadieh[52] in the past and Passalacqua and Marmo[27,53] and Ray et al.[55] in more recent years.

Although most of the CFD models simulate the bubbling fluidization regime, 2D computational domains have been used to study FBRs operated under different conditions and other fluid-dynamics regimes. Wu and Li[65] built a 2D computational fluid dynamics-discrete phase model (CFD–DPM) simulation setup to study a novel drag force model in the fast fluidization regime, while Li and Kuipers[64,67] studied the gas–solid flow behavior and regime transition in 2D and 3D geometries coupling CFD to a Lagrangian solution for the granular phase.

The overall height of the cylindrical reactor is 4.347 m, with diameter of the lower region of 700 mm and diameter of the upper part of 1400 mm. A disengagement conic zone is present to gradually enlarge the cross-section area and reduce the gas velocity, thus preventing solid elutriation and keeping all particles within the polymerization zone. The real system is fed by a gas stream through a distributor plate that is omitted in the computational model. The mesh size has been chosen after achieving grid-independent results, with the aim of finding the grid with the best trade-off between the numerical error reduction and the need of reproducing the literature reference results at a reasonable computational cost. Data are therefore obtained with a 2D planar mesh composed by 225 500 high-quality elements with the maximum aspect ratio of 1.53 (1 – optimum) and the maximum skewness of 0.13 (0 – best, 1 – worst). The chosen mesh gives a particle-to-grid ratio $\mathcal{P}$ of about 0.22 for 669 μm particles. The validation of the computational grid is discussed in detail in Section S2.1 of the Supporting Information attached to this work.

The multiphase mixture is composed by pressurized ethylene (gas primary phase) and high-density polyethylene (solid disperse phase). Important bulk data such as phase density (ρ), angle of repose,[56] viscosity, and coefficient of restitution (e) are listed in **Table 4**.

**ADVANCED
SCIENCE NEWS**

www.advancedsciencenews.com

[M] acro-
molecular

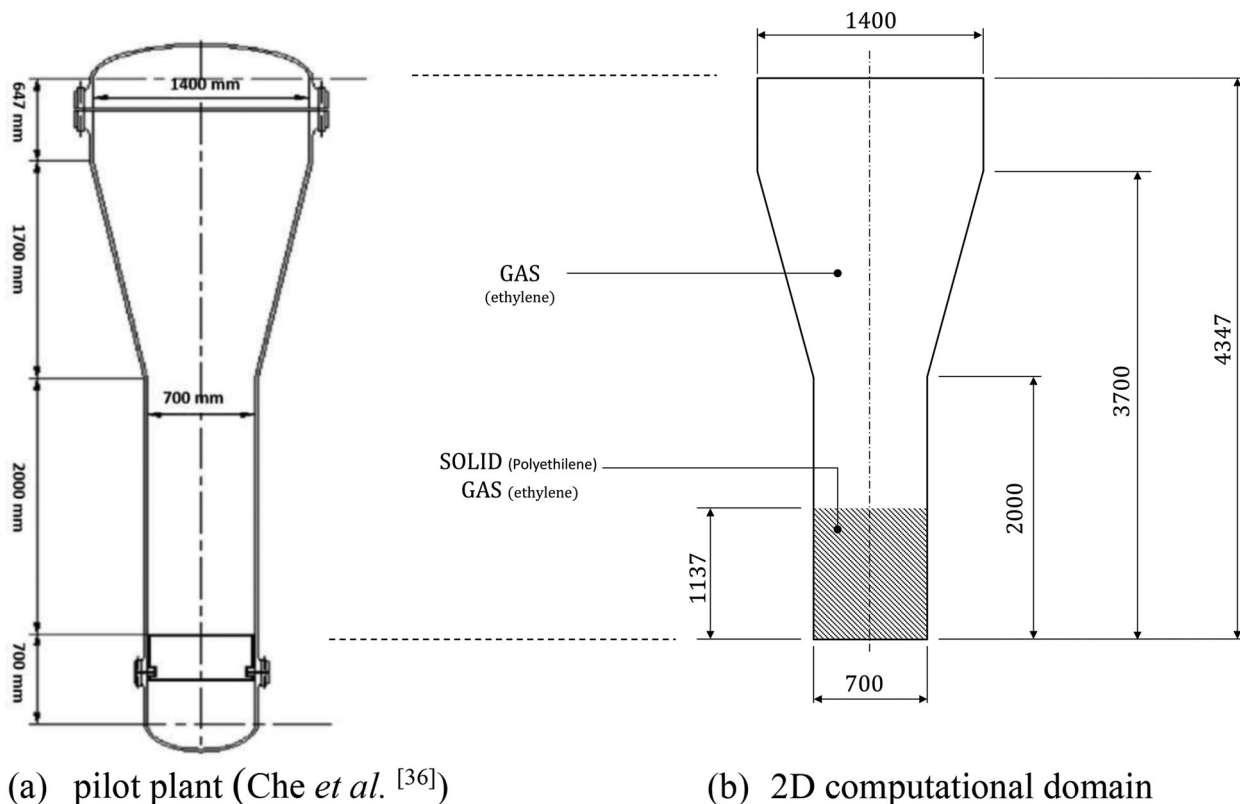Reaction Engineering
www.mre-journal.de

Figure 2. Schematic representations a) of the pilot-scale reactor and b) of the corresponding 2D computational domain. Figure a reproduced with permission.[36] Copyright 2015, Elsevier.

Table 4. Material properties at $T = 361$ K and $P = 2$ MPa (viscosity data taken from Che et al.[36]). KTGF stands for kinetic theory of granular flows.

	ρ [kg m^{-3}]	Angle of repose [–]	μ [Pa s]	E [–]
Ethylene (g)	20.2	–	$1.72 \cdot 10^{-5}$	–
Polyethylene (s)	918	30	KTGF	0.9

The fluidization characteristics of the system have been studied for three different uniform inlet gas velocities, 20, 40, and 61 cm s^{-1}. Solid volume fraction and velocity magnitude data were compared quantitatively by averaging results in time for 50 s of operation. In order to exclude the highly transient start-up of the flow motion and to obtain quasi-steady-state results, the first 10 s of fluidization data were discarded and the averaging procedure was conducted between 10 and 60 s of physical time. The validation of the multiphase simulation model is described in Section S2 of the Supporting Information provided with this work, while the averaging technique is described in detail in the next section.

4.2. Analysis Methodology and Definition of Simulation Cases

The comparison of the results obtained by the two modeling approaches, detailed CFD and simplified SCM, was carried out in

terms of selected properties at different reactor heights, specifically considering four sampling lines placed in the lower cylindrical part of the reactor, as depicted in **Figure 3**.

Equations (41) and (42) show the relations used to average in time the local and average solid volume fraction

$$\alpha_\theta^j = \alpha_s^j = \frac{1}{n} \sum_{i=\mathrm{dt_{init}}}^{\mathrm{dt_{end}}} \alpha_s^{j,i} \tag{41}$$

where n is the total number of time steps evaluated between time $t = 10$ s ($\mathrm{dt_{init}} = 10\,000$) and $t = 60$ s ($\mathrm{dt_{end}} = 60\,000$). Data were sampled every 100 time steps, j specifies the computational grid cell while i the time step. Cell-centered values α_s^j were then averaged in space to obtain the mean solid volume fraction as a function of the reactor height $\alpha_{s,ave}$. The average gas volume fraction was obtained observing that the total volume has to complement to 1

$$\alpha_{\theta,ave} = \alpha_{s,ave} = 1 - \alpha_{g,ave} \tag{42}$$

The simulation cases were defined by given set of initial conditions, for both monodisperse and polydisperse populations of particles. Their primary aim was to compare the fluidization properties predicted by the detailed CFD model with those coming from the simplified compartmentalized model. Monodisperse cases were also used to identify proper CFD simulation
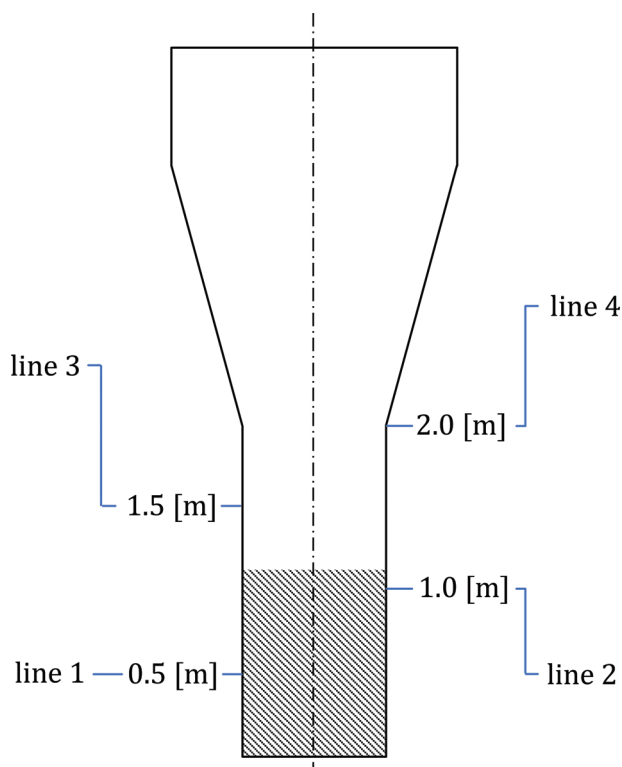
**ADVANCED
SCIENCE NEWS**

www.advancedsciencenews.com

**[M]acro-
molecular
Reaction Engineering**

www.mre-journal.de

Figure 3. Scheme of the inspection lines used for the quantitative analysis.

conditions comparing these results with literature ones (Che et al.[36]). The investigated simulation parameters were:

1) particle average diameter, to study the effect of particles inertia;
2) standard deviation of the particle size distribution, to study the effect of populations polydispersity;
3) solid initialization height, to understand the influence that the quantity of particles loaded into the reactor at the beginning has on solid expansion;
4) gas velocity, to investigate the influence of the carrier stream on the drag exerted on particles and verify the absence of elutriation.

Besides the mutiphase flow model validation, described in detail in the next section, an accurate comparison with literature results has been carried out regarding the computational grid construction and the equations discretization order (Section S2.1, Supporting Information), the geometric description (Section S2.2, Supporting Information), and the initial conditions (Section S3, Supporting Information). All the material is reported in the Supporting Information attached to this work.

4.3. Assessment of the Interaction Effects

The actual relevance of including the mutual interaction effects induced by the presence of the particulate phase on the gas flow has been investigated by assessing the importance of the Simonin model in transport equations for turbulence (Π_{k_g} in Equa-

tion (9) and Π_{ε_g} in Equation (10)). The analysis is performed by comparing the contours at different physical times (**Figure 4**) and the time-averaged cell-centered data (**Figure 5**) of the solid volume fractions reported by Che et al.[36] with those resulting from a simulation without and with turbulent interaction modeling.

The best reproduction of literature results was achieved using the Simonin model for turbulent interaction. Therefore, such contribution is essential to predict the correct fluidization in terms of gas bubble formation and solid phase mixing and it is used in all simulations reported in the following section. Moreover, the quantitative data reported in Figure 5 support such statement. The agreement is always quite good when interaction is accounted for, especially at the top of the cylindrical part of the reactor.

5. Results

5.1. Fluidization Regime

In order to compare the two modeling approaches, CFD and SCM, the steady-state conditions established inside a fluidized bed reactor at constant gas flowrate and holdup of a solid phase with given particle size distribution are examined. As anticipated, we focus on bed expansion only, assuming no solid elutriation, no reaction, and no solid injection or withdrawal in addition to the initially charged amount. The same reactor geometry used in the previous section to validate the CFD numerical setup is selected for the sake of convenience (see Figure 2). Note that a simpler cylindrical geometry is considered in the SCM case: this means that only the bottom part of the reactor is simulated, with height (and therefore number of compartments) large enough to contain the amount of solid initially charged to the reactor in the CFD case. Since the solid entrainment is minimal at the selected conditions (i.e., a minor amount of solid is filling the conical region and most remains in the lower-cylindrical portion where the most interesting fluidization phenomena occur; see contours of Figure 4), the comparison remains meaningful despite such difference in geometry.

The parameter values and operating conditions of all examined cases are summarized in **Table 5**. According to Geldart classification,[48-50] the solid phase is composed of particles A–B type, that is representative of polyethylene produced in gas phase by catalytic polymerization. Note that both the cases of particles with homogeneous (monodisperse) and heterogeneous size distribution (polydisperse) are considered, to better elucidate the interplay between particle size distribution and solid segregation along the reactor axis.

About the selected range of gas flows, it has been restricted to realistic values large enough to establish fluidization conditions as well as small enough to prevent solid loss by elutriation. More specifically, with reference to the fluidization regimes according to Kunii and Levenspiel[1] (Chapter 3, Figure 16b), the range of examined operating conditions can be represented in terms of the two dimensionless variables $d_p^* = Ar^{1/3}$ and $u^* = Re_p/Ar^{1/3}$, where Ar and Re_p are Archimedes and particle Reynolds number, respectively. This is shown in **Figure 6**, where the explored region is indicated by the orange square (dashed edges), restricted to the subregion with continuous edges to remain inside the so-called
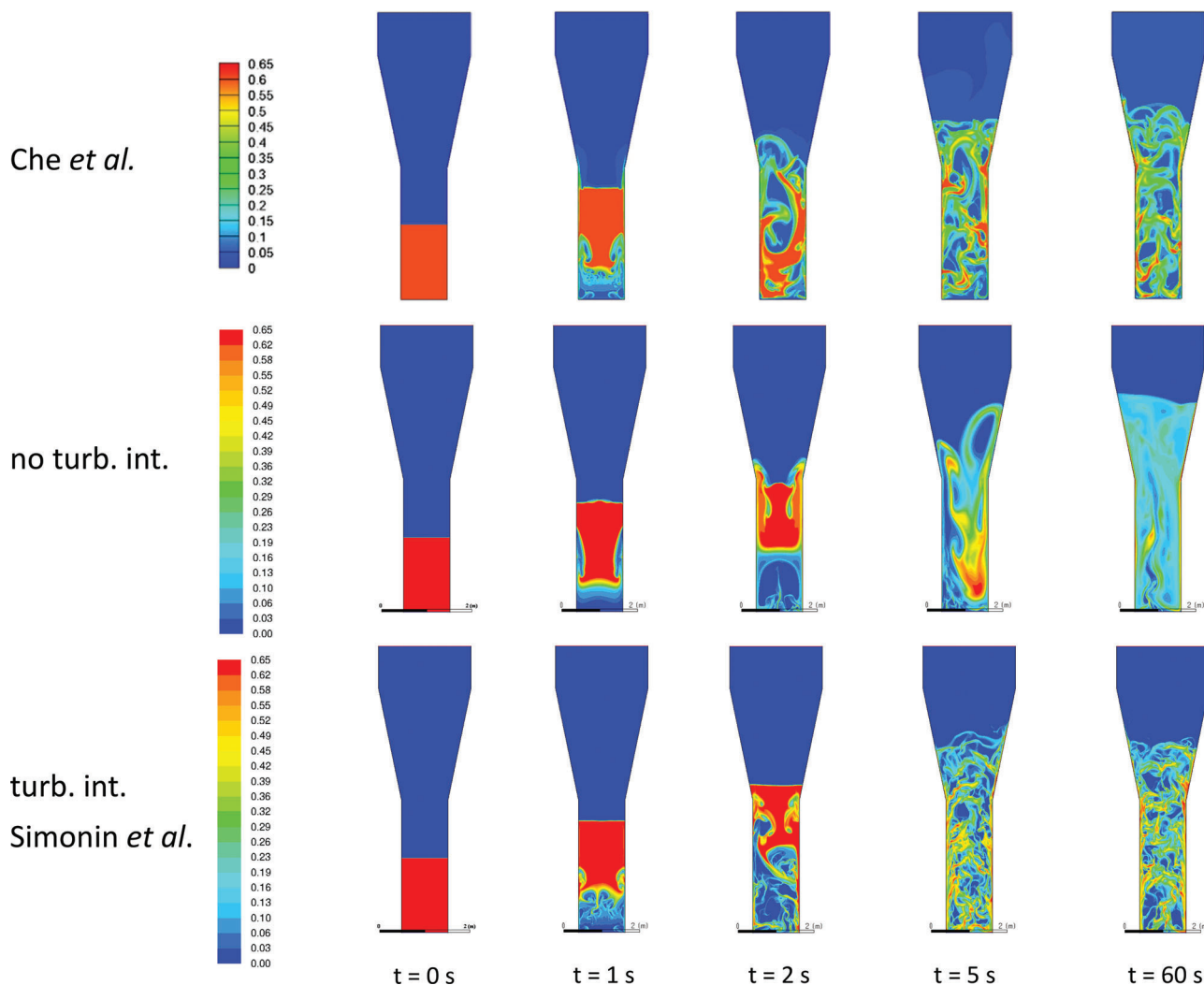
**ADVANCED
SCIENCE NEWS**

www.advancedsciencenews.com

Macro-
molecular
Reaction Engineering
www.mre-journal.de

Figure 4. Comparison between the solid volume fraction contours, at different physical times, for the reference case (courtesy of Che et al.[36]), a case without any interaction and a case with the Simonin and Viollet[38] interaction model. Monodisperse particles with size $d = 446$ µm, fine computational grid (cf. Section S2.1 of Supporting Information). Top image reproduced with permission.[36] Copyright 2015, Elsevier.

"bubbling" regime, which is the region of applicability of the simplified fluid dynamic relationships listed in Table 3.

The simulation results for all cases are presented below, first considering the monodisperse cases and then those involving solid phases with particle size distribution with different broadenings. The comparisons are carried out in terms of axial profiles of solid volume fraction (α_θ) and average particle size ($\bar{d}_p$). In the SCM case, compartment-average particle sizes are considered (number average of the weight size distribution of the compartment); in the CFD case, such average quantities have been evaluated according to Equations (41) and (42) to obtain time and space average values inside the reactor.

5.2. Monodisperse Cases

Three different cases have been considered, with particle size equal to 223, 446, and 669 µm, respectively, and gas velocity rang-

ing from 10 to 61 cm s^{-1} depending upon the specific particle size under examination (for example, gas velocity larger than 20 cm s^{-1} cannot be used with the smallest particle size because there would be too much solid entrainment). In all cases, the entire cylindrical region (2 m high) was initially filled with the solid particles at solid volume fraction typical of a fixed bed, $\alpha_\theta = 0.63$ (cf. Section S3 in the Supporting Information). The results of the two models are compared in **Figure 7** in terms of radial average volume fraction of solid phase at different positions along the reactor axis inside the cylindrical portion starting from 0.5 m distance from the gas distributor. Positions closer to the first part of the reactor were not considered because of too close to the distributor: since completely different representations of the gas inlet region have been implemented in the two models, the resulting differences in the predicted fluid flow field prevent a fair comparison close to the reactor bottom.

Results indicate very good agreement between SCM and CFD predictions, especially considering the huge difference in
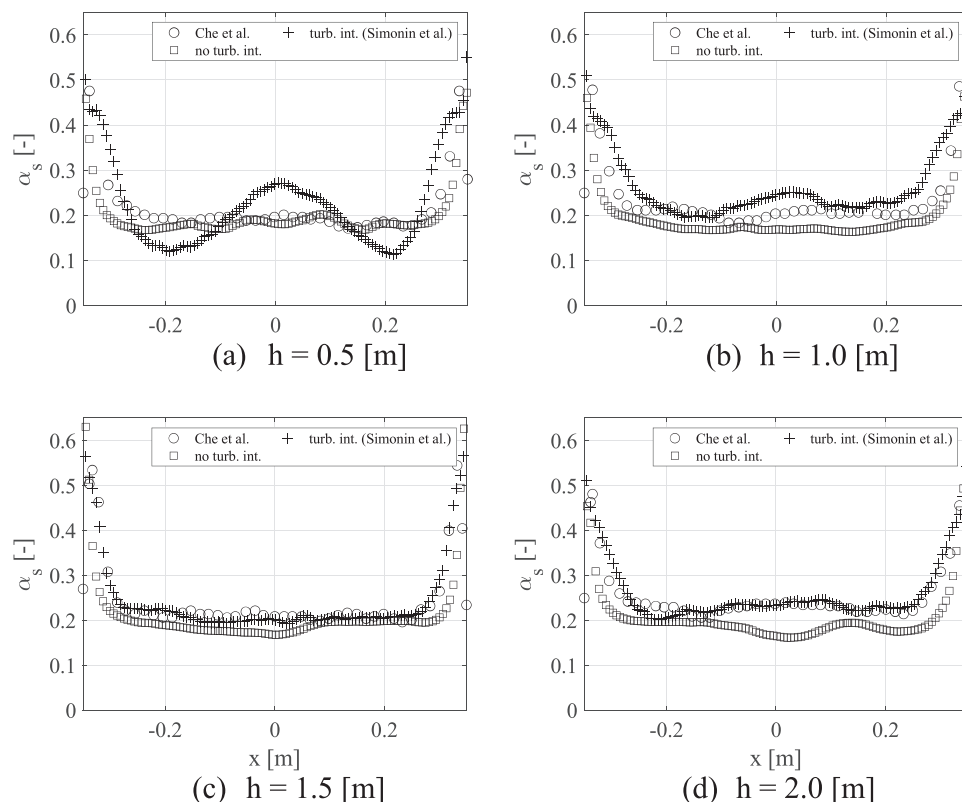
ADVANCED
SCIENCE NEWS
www.advancedsciencenews.com

[M] acro-
molecular
Reaction Engineering
www.mre-journal.de

Figure 5. Comparison between the time-averaged cell-centered data of solid volume fraction at different reactor heights (h = 0.5 (a), 1.0 (b), 1.5 (c) and 2.0 m (d)) for the reference case (courtesy of Che et al.[36]), a case without any interaction and a case with the Simonin and Viollet[38] interaction model. Monodisperse particles with size d = 446 µm. Monodisperse particles with size d = 446 µm, fine computational grid (cf. Section S2.1 in the Supporting Information).

Table 5. Parameter values and operating conditions used in all examined cases.

ρ_g [kg m^{-3}]	ρ_s [kg m^{-3}]	W (t = 0 s) [kg]	d_p [µm]	u_g [cm s^{-1}]
20	900	790	100–700	10–60

computational effort between the two cases. As expected, the bed expansion increases at increasing gas velocity, while the solid volume fraction increases in all cases at increasing height inside the reactor. In quantitative terms, the values of average discrepancy between the two predictions range from 7% to 19%, with an average value of ≈10% and the maximum error obtained for small particles at very low fluidization velocities in the upper part of the reactor (d = 223 µm, u_g = 10 cm s^{-1}, h = 2 m). This is due to the fact that such small velocities are just sufficient to fluidize the bed but particles are not expanded and the solid remains packed.

5.3. Polydisperse Cases

Another set of comparative simulations has been carried out considering solid particles with different size distributions. Specifically, Gamma distribution was assumed in three cases, consid-

ering two values of average particle size (d_{ave}) and distribution variance (σ)

$$f(d) = \frac{\beta^\alpha}{\Gamma(\alpha)} d^{\alpha-1} e^{-\beta d} \tag{43}$$

where $\Gamma(\alpha)$ is the Gamma function and the characteristic parameters are $\alpha = d_{ave}^2/\sigma$ and $\beta = d_{ave}/\sigma$. As representative of solid phases with a very broad distribution, a fourth case was also examined corresponding to a mixture of three monodisperse particles each one with the same mass fraction.

While size distributions were readily accounted for in SCM (as $w_{tot}(r)$ in Equation (29)), in the CFD case, the method presented by Marchisio et al.[57-59] was used to calculate a three node quadrature (with nodes indicated with indexes QP0, QP1, and QP2) with Direct Quadrature Method of Moments (DQMOM) approach. The first six moments of the distributions are used to retrieve quadrature quantities, i.e., weights (α_θ) and abscissas ($\alpha_\theta L_\theta$) through the Wheeler moment inversion algorithm[60] and such diameters are assigned to the different nonreactive solid phases (each one advected with its own velocity) to account for polydispersity.

The specific numerical values of all these parameters are summarized in **Table 6**. To better understand the different size distributions of the solid phase initially charged to the reactor in the first three cases, they are shown in **Figure 8**.

**ADVANCED
SCIENCE NEWS**

www.advancedsciencenews.com

{M}acro-
molecular
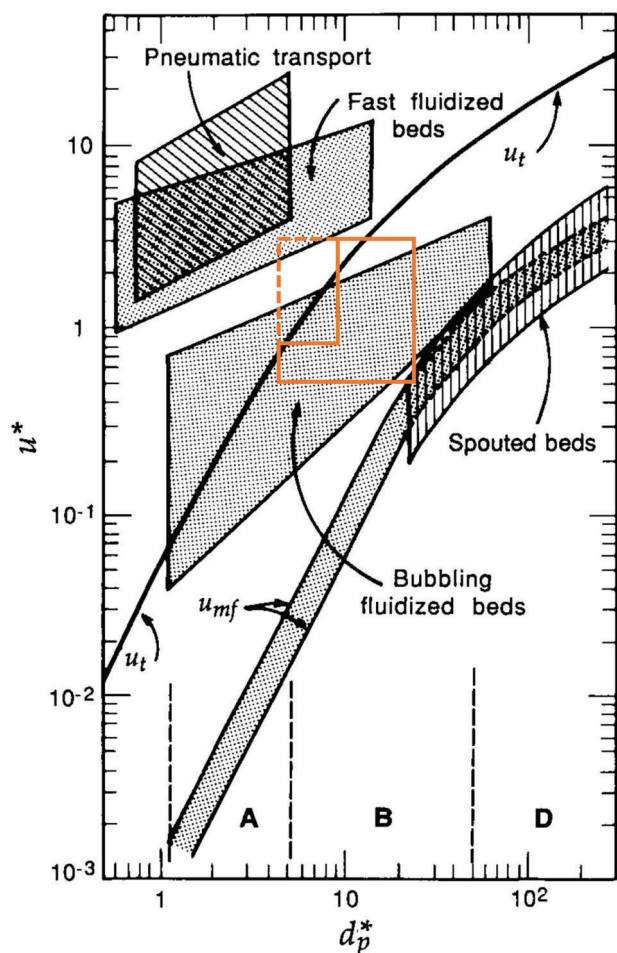Reaction Engineering

www.mre-journal.de

Figure 6. Particle fluidization regimes according to Kunii and Levenspiel.[1] The region marked in orange defines the regime explored with simulations. Reproduced with permisison.[1] Copyright 1991, Elsevier.

The comparisons between the predictions of the two approaches, SCM and CFD, for the first three cases, 01-p to 03-p, are shown in **Figures 9** and **10**. In terms of solid volume fraction (Figure 9), the SCM predicted values are typically larger than the CFD ones, with average error below 15% but the maximum errors up to 29% at the largest gas velocity. The agreement is improving at increasing average particle size, where the errors remain below 10% in all cases. Therefore, the discrepancy could be imputed to the tail of the smallest particles in the distributions: such particles are Geldart type A and the applicability of the simplified fluid dynamic equations in Table 3 could be questionable, especially at high gas velocity. The comparison is much better in terms of average particle sizes (Figure 10): not only the discrepancy is below 1% in all cases but the (limited) solid segregation is invariably well predicted, with the expected accumulation of larger particles at the reactor bottom. Such segregation is anyhow minor in all cases, i.e., the gas velocity is large enough to ensure very good mixing in all cases, thus pushing the reactor toward well mixed conditions.

In the most heterogeneous case of trimodal particle size distribution (04-p in Table 6), the same kind of behavior is found,

as described by **Figure 11**, with a limited overestimation of the solid volume fraction by the SCM (average error 13%) and of the variation of particle size with the reactor height (average error of ≈1%).

The values of all the predictions of both models for all conditions are specified in tabular form in Table S3 of Section S4 in the Supporting Information. Overall, the agreement between the fully detailed CFD model and the oversimplified compartmentalized model for the average size is good, with an average error of about 1% and a maximum error measured on solid volume fraction of about 15–20%. Even though the description of the complex gas–solid flow field established in this type of reactors based on the semiempirical relationships available in the literature should be checked for the specific solid and operating conditions under examination, it appears appropriate to study reactive systems at a modest computational cost.

The difference in computational effort between the two approaches is huge: SCM provides steady-state results in about 5 min of computational time running in serial mode on an Intel i5 laptop CPU (central processing unit), while the detailed multiphase CFD simulation of the FBR quasi-steady-state operation is obtained in about 5–7 days of computational on a 16 cores (Intel Xeon E5-2697v2 processors – 2.7 GHz nominal, 3.0–3.5 GHz peak) node of the ETHZ Euler cluster.

The combination between detailed CFD simulations and any model based on such simplified descriptions implemented here is a feasible approach in this direction.

6. Conclusions

Focusing on the fluidization behavior of nonreactive Geldart-type A–B particles in steady-state FBRs, a model comparison has been carried out. Namely, the predictions of a 2D multifluid CFD model and of a 1D compartmentalized model with simplified fluid dynamics description are compared in terms of steady-state solid distribution inside the reactor operated in batch and without reaction (pure fluidization). The multiphase CFD model setup has been first validated against relevant literature data. A proper analysis has been carried out to identify the best numerical setup and suitable initial conditions.

Monodisperse and polydisperse populations of solid particles have been studied at different gas velocities to assess the prediction capabilities of the simplified approach. The results show that the semiempirical fluid dynamic description typically used in SCM is adequate to properly describe the fluidization behavior of solid monodisperse particles in terms of solid volume fraction distribution, with errors smaller than 20% in all cases. When considering broad size distributions, particle segregation is very well predicted in terms of average volume fraction, with discrepancy between the two models between 15% and 30%. The agreement is even better in terms of average diameters along the reactor axis (mean error below 1%), also in the case of very broad size distributions.

SCM is in principle applicable to any fluidization regime if an appropriate fluid-dynamic description is available.

Overall, these results support the use of compartmentalized models to predict the fluidization behavior of nonreactive, polydisperse particles in FBRs at operating conditions typical of
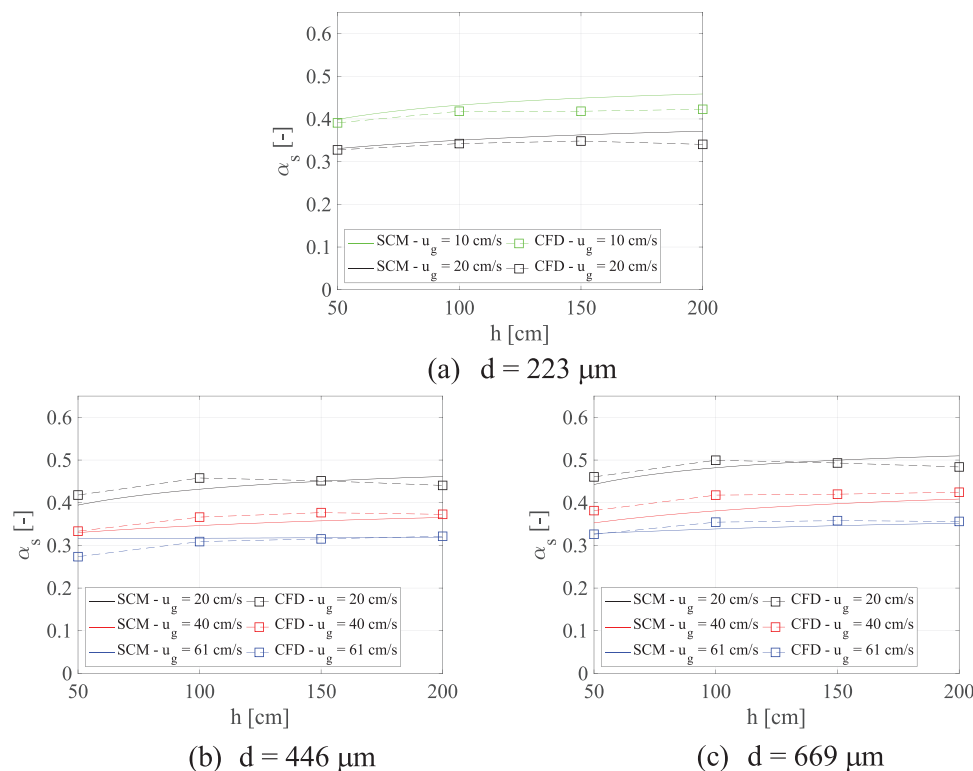
ADVANCED
SCIENCE NEWS
www.advancedsciencenews.com

{M} acro-
molecular
Reaction Engineering
www.mre-journal.de

(a) d = 223 μm

(b) d = 446 μm

(c) d = 669 μm

Figure 7. Comparison between the time- and space-averaged cell-center data (CFD) and compartment data (SFD) of solid volume fraction at different reactor positions for different particle diameters.
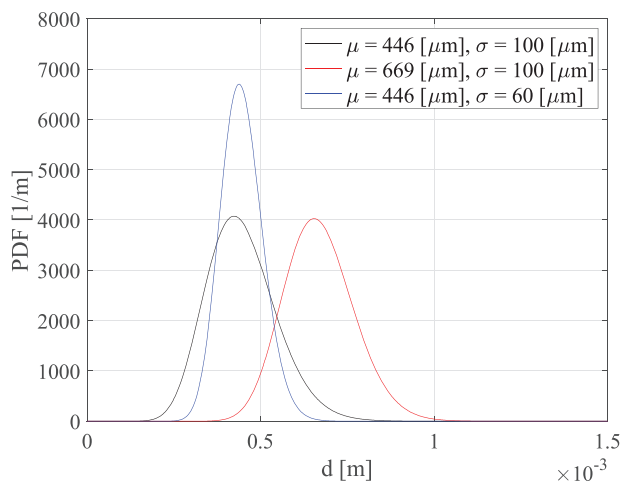

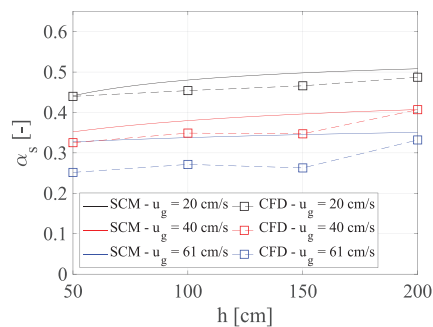**Figure 8.** Graphic representation of the Gamma distributions tested.

Table 6. Parameters and quadrature approximation values of Gamma distribution tested (01-p to 03-p) and heterogeneous three-modal distribution function (04-p).

Case	d_{ave} [μm]	σ [μm]	L_θ [μm]	α_θ [−]
01-p	446	100	QP0: 559.40	QP0: 0.1654
			QP1: 408.51	QP1: 0.4100
			QP2: 262.81	QP2: 0.0546
02-p	669	100	QP0: 830.09	QP0: 0.1437
			QP1: 644.05	QP1: 0.4157
			QP2: 488.01	QP2: 0. 0706
03-p	446	60	QP0: 543.50	QP0: 0.1396
			QP1: 432.53	QP1: 0.4165
			QP2: 337.75	QP2: 0.0739
04-p	500	–	QP0: 800.00	QP0: 0.2100
			QP1: 500.00	QP1: 0.2100
			QP2: 200.00	QP2: 0.2100

polyolefin production and with computational effort negligible with respect to CFD simulations. The latter, indeed, needs days of simulation, while the compartment-based approach provides steady-state results in few minutes of computing.

Supporting Information

Supporting Information is available from the Wiley Online Library or from the author.

ADVANCED
SCIENCE NEWS
www.advancedsciencenews.com

acro-
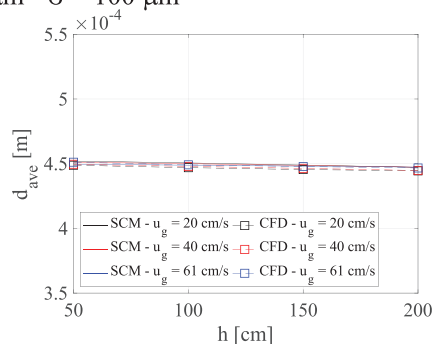olecular
Reaction Engineering
www.mre-journal.de
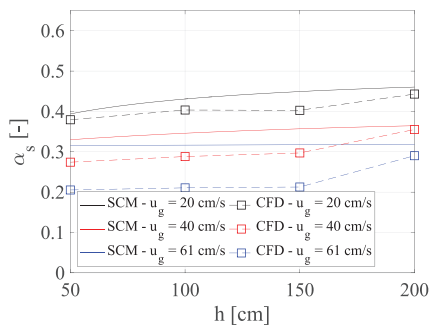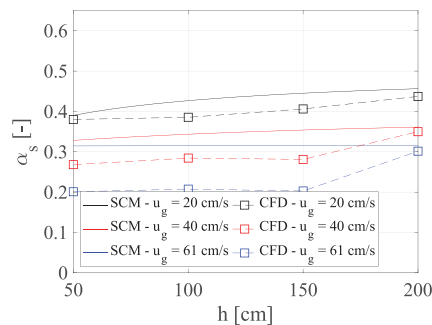
Figure 9. Comparison between the time- and space-averaged cell-center data (CFD) and compartment data (SFD) of solid volume fraction at different reactor positions for different distributions.
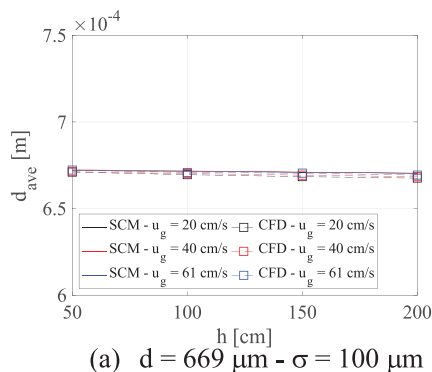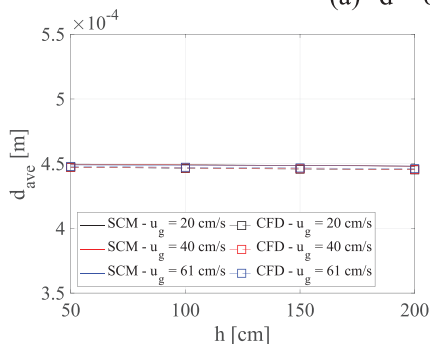
Figure 10. Comparison between the time- and space-averaged cell-center data (CFD) and compartment data (SFD) of particles average diameter at different reactor positions for different distributions.
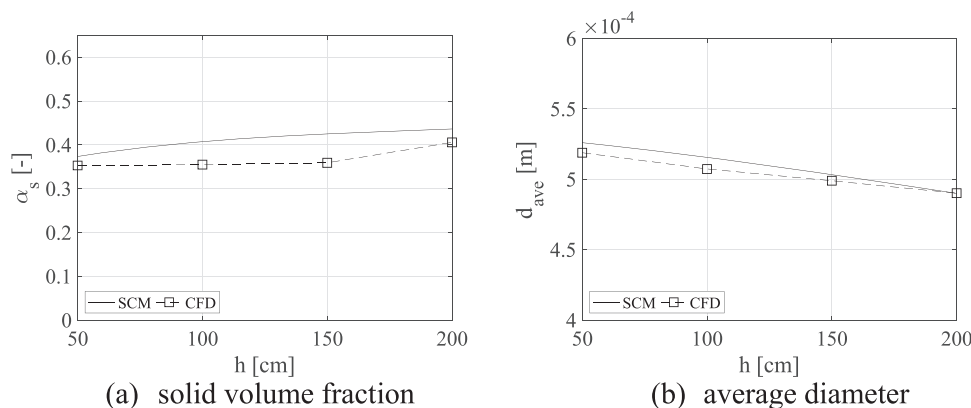
**ADVANCED
SCIENCE NEWS**

www.advancedsciencenews.com

**[M]acro-
molecular**

Reaction Engineering

www.mre-journal.de

Figure 11. Comparison between the time- and space-averaged cell-center data (CFD) and compartment data (SFD) of a) solid volume fraction and b) average particle diameter at different reactor positions for a distribution built with $d_0 = 800$ μm/$\alpha_0 = 0.21$; $d_1 = 500$ μm/$\alpha_1 = 0.21$; $d_2 = 200$ μm/$\alpha_2 = 0.21$.

Conflict of Interest

The authors declare no conflict of interest.

Data Availability Statement

The data that support the findings of this study are available from the corresponding author upon reasonable request.

Keywords

CFD two-fluid model, compartmentalized model, fluidized bed reactors, simplified fluid-dynamics

Published online:

[1] D. Kunii, O. Levenspiel, *Fluidization Engineering*, 2nd ed., Butterworth-Heinemann, Oxford **1991**.

[2] R. F. Alves, T. Casalini, G. Storti, T. F. L. Mckenna, *Macromol. React. Eng.* **2021**, *15*, 2000059.

[3] J. B. P. Soares, T. F. L. McKenna, *Pololefin Reaction Engineering*, Wiley-VCH, Weinheim **2012**.

[4] K. B. Mcauley, J. P. Talbot, T. J. Harris, *Chem. Eng. Sci.* **1994**, *49*, 2035.

[5] G. Dompazis, A. Roussos, V. Kannellopoulos, C. Kiparissides, *Comput.-Aided Chem. Eng.* **2005**, *20*, 427.

[6] M. R. Abbasi, A. Shamiri, M. A. Hussain, *Rev. Chem. Eng.* **2019**, *35*, 311.

[7] M. An, X. Guan, N. Yang, *Chem. Eng. Sci.* **2020**, *223*, 115743.

[8] A. Sriniketh, B. Ashraf Ali, *Chem. Eng. Commun.* **2021**, *208*, 843.

[9] H. Hatzantonis, A. Goulas, C. Kiparissides, *Chem. Eng. Sci.* **1998**, *53*, 3251.

[10] M. Alizadeh, N. Mostoufi, S. Pourmahdian, R. Sotudeh-Gharebagh, *Chem. Eng. J.* **2004**, *97*, 27.

[11] O. Ashrafi, H. Nazari-Pouya, N. Mostoufi, R. Sotudeh-Gharebagh, *Adv. Powder Technol.* **2008**, *19*, 321.

[12] R. F. Alves, T. F. L. Mckenna, *Ind. Eng. Chem. Res.* **2021**, *60*, 11977.

[13] T. F. Mckenna, J. B. P. Soares, *Chem. Eng. Sci.* **2001**, *56*, 3931.

[14] B. Elvers, *Ullmann's Encyclopedia of Industrial Chemistry*, Verlag Chemie, Hoboken, NJ **1991**.

[15] B. G. M. van Wachem, J. C. Schouten, C. M. van Den Bleek, R. Krishna, J. L. Sinclair, *AIChE J.* **2001**, *47*, 1035.

[16] K. W. Chu, B. Wang, D. L. Xu, Y. X. Chen, A. B. Yu, *Chem. Eng. Sci.* **2011**, *66*, 834.

[17] G. N. Ahuja, A. W. Patwardhan, *Chem. Eng. J.* **2008**, *143*, 147.

[18] X.-Z. Chen, Z.-H. Luo, W.-C. Yan, Y.-H. Lu, I.-S. Ng, *AIChE J.* **2011**, *57*, 3351.

[19] W.-C. Yang, J. Li, Z. H. Luo, *Powder Technol.* **2012**, *231*, 77.

[20] E. Askari, P. Proulx, A. Passalacqua, *ChemEngineering* **2018**, *2*, 8.

[21] K. Hayashi, H. Nakamura, S. Watano, *Powder Technol.* **2020**, *360*, 1321.

[22] S. Hu, X. Liu, *Chem. Eng. J.* **2020**, *383*, 123122.

[23] Y. Lu, J. Huang, P. Zheng, *Chem. Eng. J.* **2015**, *274*, 123.

[24] S. Wang, K. Luo, C. Hu, J. Lin, J. Fan, *Chem. Eng. Sci.* **2019**, *197*, 280.

[25] S. Hu, X. Liu, *Chem. Eng. J.* **2021**, *413*, 127503.

[26] H. Arastoopour, D. Gidaspow, R. W. Lyczkowski, *Transport Phenomena in Multiphase Systems*, Springer, Berlin **2021**.

[27] E.-U. Hartge, L. Ratschow, R. Wischnewski, J. Werther, *Particuology* **2009**, *7*, 283.

[28] C. Loha, H. Chattopadhyay, P. K. Chatterjee, *Chem. Eng. Sci.* **2012**, *75*, 400.

[29] S. Chapman, T. G. Cowling, *The Mathematical Theory of Non-Uniform Gases*, Cambridge University Press, Cambridge, UK **1961**.

[30] J. T. Jenkins, S. B. Savage, *J. Fluid Mech.* **1983**, *130*, 187.

[31] C. K. K. Lun, S. B. Savage, D. J. Jeffrey, N. Chepurniy, *J. Fluid Mech.* **1984**, *140*, 223.

[32] P. C. Johnson, R. Jackson, *J. Fluid Mech.* **1987**, *176*, 67.

[33] D. Gidaspow, *Multiphase Flow and Fluidization: Continuum and Kinetic Theory Description*, Academic Press, Cambridge, MA **1994**.

[34] D. G. Schaeffer, *J. Differ. Equations* **1987**, *66*, 19.

[35] *ANSYS Fluent Theory Guide*, ANSYS, Inc., Canonsburg, PA **2017**.

[36] Y. Che, Z. Tian, Z. Liu, R. Zhang, Y. Gao, E. Zou, S. Wang, B. Liu, *Powder Technol.* **2015**, *278*, 94.

[37] Z. Naumann, L. Schiller, *Z. Ver. Dtsch. Ing.* **1935**, *77.318*, e323.

[38] O. Simonin, P. L. Viollet in Proc. Numerical Methods Multiphase Flows, ASME, New York 1990, pp. 65–82.

[39] B. E. Launder, D. B. Spalding, *Comput. Methods Appl. Mech. Eng.* **1974**, *3*, 269.

[40] S. V. Patankar, D. B. Spalding, in *Numerical Prediction of Flow, Heat Transfer, Turbulence and Combustion*, Pergamon, Oxford **1983**, p. 54.

[41] S. Vasquez, presented at ASME 200 Fluids Engineering Division Summer Meeting, **2000**.

[42] T. J. Barth, D. C. Jespersen presented at 27th Aerospace Science Meeting, Reno, NV, USA. 1989.

[43] C. M. Rhie, W. L. Chow, *AIAA J.* **1983**, *21*, 1525.

[44] K.-Y. Choi, W. H. Ray, *Chem. Eng. Sci.* **1985**, *40*, 2261.

[45] K. Y. Choi, X. Zhao, S. Tang, *J. Appl. Polym. Sci.* **1991**, *53*, 1589.

[46] J. Y. Kim, K. Y. Choi, *Chem. Eng. Sci.* **2001**, *56*, 4069.

[47] J. Y. Kim, K. Y. Choi, *AIChE Symp. Ser.* **1999**, *95*, 77.

[48] D. Kunii, O. Levenspiel, *AIChE Symp. Ser.* **1991**, *95*, 77.

[49] D. Geldart, A. C. Y. Wong, *Chem. Eng. Sci.* **1984**, *39*, 1481.

[50] D. Geldart, A. C. Y. Wong, *Chem. Eng. Sci.* **1985**, *40*, 653.

[51] H. I. de Lasa, *Chemical Reactor Design and Technology*, Nato ASI Series, Series E: Applied Sciences, Vol. *110*, Springer, Berlin **2012**.

[52] D. Gidaspow, B. Ettehadieh, *Ind. Eng. Chem. Fundam.* **1983**, *22*, 193.

[53] A. Passalacqua, L. Marmo, *Chem. Eng. Sci.* **2009**, *64*, 2795.

[54] M. Ray, F. Chowdhury, A. Sowinski, P. Mehrani, A. Passalacqua, *Chem. Eng. Sci.* **2019**, *197*, 327.

[55] D. Geldart, *Powder Technol.* **1973**, *7*, 285.

[56] H. M. Beakawi Al-Hashemi, O. S. Baghabra Al-Amoudi, *Powder Technol.* **2018**, *330*, 397.

[57] D. L. Marchisio, J. T. Pikturna, R. O. Fox, R. D. Vigil, A. A. Barresi, *AIChE J.* **2003**, *49*, 1266.

[58] D. L. Marchisio, R. D. Vigil, R. O. Fox, *Chem. Eng. Sci.* **2003**, *58*, 3337.

[59] D. L. Marchisio, R. D. Vigil, R. O. Fox, *J. Colloid Interface Sci.* **2003**, *258*, 322.

[60] D. L. Marchisio, R. O. Fox, *Computational Models for Polydisperse Particulate and Multiphase Systems*, Cambridge University Press, Cambridge **2010**.

[61] S. E. Elghobashi, *Phys. Fluids* **1983**, *26*, 931.

[62] G. Wu, Y. Li, *Processes* **2021**, *9*, 1574.

[63] J. Li, J. A. M. Kuipers, *Powder Technol.* **2002**, *127*, 173.

[64] B. P. B. Hoomans, *Ph.D. Thesis*, University of Twente, Netherlands **2000**.